Preprint of OMAE2018-77804

6-DOF HYDRODYNAMIC MODELLING FOR WIND TUNNEL HYBRID/HIL TESTS OF FOWT: THE REAL-TIME CHALLENGE

Ilmas Bayati *
Mechanical Engineering
Politecnico di Milano
Via La Masa, 1, 20156, Milano
Email: ilmasandrea.bayati@polimi.it

Alan Facchinetti
Mechanical Engineering
Politecnico di Milano
Via La Masa, 1, 20156, Milano
alan.facchinetti@polimi.it

Alessandro Fontanella
Mechanical Engineering
Politecnico di Milano
Via La Masa, 1, 20156, Milano
alessandro.fontanella@polimi.it

Marco Belloli
Mechanical Engineering
Politecnico di Milano
Via La Masa, 1, 20156, Milano
marco.belloli@polimi.it

ABSTRACT

This paper deals with the numerical approach and technical implementation of the 6-DoF hydrodynamic modelling, combined with the Politecnico di Milano HexaFloat robot, adopted for wind tunnel Hybrid/HIL tests floating offshore wind turbines. The hybrid testing methodology, along with its ocean-basin counterpart, is currently being considered as a valuable upgrade in the model scale experiments, for its capability to get rid of the typical scaling issues of such systems. The work reports an overview of the setup, the general testing methodology, presenting the main challenges about the deployment on the real-time hardware, summarizing the key solving choices. A set of results related to code-to-code comparison between the optimized HIL numerical model and the reference FAST computations are included, confirming the correctness of the approach.

NOMENCLATURE

DoF Degree of freedom
HIL Hardware-In-the-Loop
RT Real Time
IPC Individual Pitch Control
FOWT Floating Offshore Wind Turbines
PoliMi Politecnico Milano
SWE Stuttgart University Wind Energy
HexaFloat 6-DoF PoliMi parallel kinematic robot
CoG Center of Gravity
FAST Reference open-source aeroelastic computer-aided engineering tool for horizontal axis wind turbines
RNA Rotor Nacelle Assembly
FL Fairleads
PSD Power Spectral Density
ODE Ordinary Differential Equation
WAMIT Wave Analysis MIT
DTU Danmarks Tekniske Universitet
$\underline{x}$ 6x1 platform displacements
$\underline{x_s}$ 6x1 simulated platform displacements
x, y, z Platform's DoF: surge, sway, heave
φ, ϑ, ψ Platform's DoF: pitch, roll, yaw
$[M_s]$ 6x6 structural mass matrix
$[A_\infty]$ 6x6 infinite-frequency hydrodynamic added mass matrix
$[R_s]$ 6x6 structural damping matrix
$[K_s]$ 6x6 structural stiffness matrix
$\underline{F}$ 6x1 external force vector

$rad, we, moor, visc$ Radiation, wave exciting, moorings, viscous
$bal, corr$ Balance, corrections
$[M_t], [K_t]$ 6x6 mass and gravitational matrix of the wind turbine scale model
b_i CoG position of the wind turbine scale model along the *i-th* axis
J Moment of inertia
g Gravity acceleration
G Center of mass of the whole floating system
$hst, grav$ Hydrostatic, gravitational
pl, to, na, ro, bot Platform, tower, nacelle, rotor, bottom
tot, ed Total, extra-diagonal
C_d, C_{ax} Platform transverse and axial hydrodynamic drag coefficients
C_{dn}, C_{dt} Mooring cable transverse and axial hydrodynamic drag coefficients
D, d Platform cylinder's and mooring cable diameters
t, r, ax tangential, radial, axial
u, v, w Wave particle velocities, along *x,y,z*
ρ_w, ρ water and mooring cable densities
m, a Mooring line segment mass and hydrodynamic added mass
E Young's Modulus
N Number of nodes dividing each mooring cable
$\underline{r}$ 9·(N-2) Vector containing the 3 *x,y,z* displacements of (N-2) internal nodes of the 3 mooring lines
I Identity matrix
$i, i \pm 1/2$ *i-th* mooring line node index and the adjacent ones
l_G, l Distance of center of mass of the whole floating structure to the origin and mooring cable element length
$\hat{\underline{e}}_z$ Unit vector in the positive z direction
$\hat{\underline{q}}$ Tangent direction at each mooring cable's node
ε Mooring cable element strain
k_{bot}, c_{bot} Sea bed bottom stiffness and damping
C_{int} Mooring cable element internal damping
$\underline{T}, \underline{C}, \underline{W}, \underline{D}_p, \underline{D}_q$ Mooring cable tension, damping, weight, viscous (transverse), viscous (tangential) force vectors due to internal nodes
$\underline{B}$ Sea bed contact force vector
$\underline{H}_s$ Significant wave height of the sea spectrum
$\underline{T}_p$ Wave peak period of the sea spectrum
μ, σ Mean value and standard deviation

INTRODUCTION

Floating offshore wind turbines are subjected to the simultaneous effect of wind and waves and the design of such floating systems requires the scale model experimental validation of the complex numerical codes describing the related dynamics. In this scenario model scale testing which combine the physical generation of wind and waves are commonly considered of questionable in the quality of measurements they can provide, since scaling factors and issues turn out to be greatly binding, [1], [2]. For this reason, recent international and European projects (e.g. LIFES50+, [3]) have been giving value to the idea of separating the wind and wave experimentations in different facilities, [4], [5] and [6], through hybrid testing, i.e. introducing via software wind actions in ocean basin experiments and/or wave actions in wind tunnel experiments. This brings about scaling issues relaxation (e.g. Froude scaling, Reynolds number, [7] and [8]) and great exploitation of the advantage of the wind and waves respectively reproduced in the dedicated ocean basin and wind tunnel facility.

Wind tunnel hybrid testing, objective of this paper, requires a real-time modelling of the hydrodynamic forces and a wind turbine physical scale model. The modelling and methodological aspects of this testing setup are herein discussed in relation to HexaFloat Hybrid/HIL system developed by the authors to be tested in the Politecnio di Milano wind tunnel, [9].

6 DOF HYBRID/HIL SETUP

In Fig.1 the wind tunnel experimental rig is reported. More specifically, it consists of two main hardware components: *(a)* the wind turbine, which is a 1/75 aeroelastic scale model of the DTU 10 MW reference wind turbine ([8], [10]). The wind turbine model has IPC capabilities [11] and, thanks to a dedicated real-time controller, offers the possibility to implement FOWT-specific control strategies [12] for experimental Hybrid/HIL validation; *(b)* the Hexafloat 6DoF robot [6] provides motion to the wind turbine model, moving its base by means of an independent real-time controller, [13], *(c)* a 6-components dynamometric balance installed between the turbine model tower base and the HexaFloat's end effector, measures the internal actions between the floater and the turbine (i.e. aerodynamic and inertial forces). The real-time integration of the equations of motion Eq.1, combining the hydrodynamic forces $\underline{F}_{hydro}$ (computed) and the aerodynamic forces $\underline{F}_{aero}$ (measured), provides the motion to the robot's end effector.

The numerical model (Eq.1) is developed in Matlab/Simulink environment and it is verified against a reference FAST model. More specifically, a set of simplifications were required to make the numerical model "lighter" and compatible with RT execution, without losing the consistency with the physical phenomena. The choices behind these simplification are reported and discussed in the paper. The numerical model is then implemented in dSPACE real-time hardware; the equations of motion Eq.1, including computations and measurements, are integrated, so that the motion along the 6 platform DoF $\underline{x} = \{x, y, z, \varphi, \vartheta, \psi\}^T$ are given to the HexaFloat controller.

The experimental validation of the methodology herein reported can be found, for a 2 DoF (x, ϑ) similar setup, in [14]

Platform mass (kg)	M_p	$2.85693e7$
Platform Center of mass (m)	Z_{pl}	-35.884
Platform Roll moment of inertia (kgm^2)	Jx_{pl}	$2.2934e10$
Platform Pitch moment of inertia (kgm^2)	Jy_{pl}	$2.2934e10$
Platform Yaw moment of inertia (kgm^2)	Jz_{pl}	$2.0224e10$
Tower mass (kg)	M_{to}	$4.3645e5$
Tower center of mass (m)	Z_{to}	63.05
Tower roll and pitch moment of inertia (kgm^2)	J_{to}	$2.7623e8$
Nacelle height (m)	Z_{na}	119
Nacelle mass (kg)	M_{na}	$4.46e5$
Nacelle pitch moment of inertia (kgm^2)	J_{na}	$73.26e5$
Rotor mass (kg)	M_{ro}	$2.306e5$
Length scale factor (-)	λ_L	75
Mass scale factor (-)	$\lambda_M = \lambda_L^3$	$421,875$
Velocity scale factor (-)	$\lambda_f = \lambda_V/\lambda_L$	$1/25$
Acceleration scale factor (-)	$\lambda_a = \lambda_L \lambda_f^2$	$1/8.3$
Force scale factor (-)	$\lambda_F = \lambda_V^2 \lambda_f^2$	$50,625$

TABLE 1. Triple-Spar/DTU 10MW floating system's properties.

and [15].

MODELLING

The floating system adopted is the open-source Triple Spar concept by SWE [16], coupled with the DTU 10 MW wind turbine, [17]. In Fig.2 a sketch of the platform and the mass distribution are reported, whereas the main structural properties can be found in Tab.1. Eq.1 represents the 6-DoF dynamics of FOWT reproduced in wind tunnel through the Hybrid/HIL setup of Fig.1.

$$[M_s + A_\infty]\,\underline{\ddot{x}} + [R_s]\,\underline{\dot{x}} + [K_s]\,\underline{x} = \underline{F}_{hydro} + \underline{F}_{aero} \tag{1}$$

where $[M_s]$ is the mass of the global floating system (see Fig.2, Eq.A.1 and A.2), which has been obtained by linearizing, the Lagrange term of the kinetic energy based on the velocity of the center of mass, as defined in Eq.A.3. $[A_\infty]$ is the infinite-frequency added mass, given as an output of the 3D panel code computation by WAMIT [18] under the assumption of potential flow, $[R_s]$ is additional linear hydrodynamic added damping [16] and $[K_s]$ the stiffness, as in Eq.2

$$[K_s] = [K_{hst}] - [K_{grav}] \tag{2}$$

composed of the hydrostatic restoring term from WAMIT [18] and gravitational one, Eq.A.6 and Eq.A.7.

Aerodynamic forces As reported in Eq.3 the aerodynamic force vector comes from the measurements provided by the balance $\underline{F}_{bal}$ to which a correction force vector $\underline{F}_{corr}$ needs to be applied.

$$\underline{F}_{aero} = \underline{F}_{bal} + \underline{F}_{corr} \tag{3}$$

More specifically, the correction force vector can be expressed as in Eq.4

$$\underline{F}_{corr} = [M_t]\underline{\ddot{x}_s} + [K_t]\underline{x}_s \tag{4}$$

where $[M_t]$ and $[K_t]$, reported in detail in Eq.A.4 and A.5, are respectively the mass and stiffness matrices of the physical scale model, defined under the hypothesis of rigid motion and small rotations. These are combined to the simulated DoF $\underline{x}_s$ to get the inertial and gravitational contributions of the model itself which are measured along with the aerodynamic forces in $\underline{F}_{bal}$, thus providing $\underline{F}_{aero}$ only. This correction is needed due to the small, altough inevitable differences in the mass properties of the model with respect to the full scale target, providing inertial and gravitational contributions of the model. As a further advantage, the presented HIL methodology allows to get rid of Froude scaling [8], enhancing the quality of scale model measurements (e.g. higher wind speed, better signal/noise ratio, Reynolds number discrepancy less penalising) but leads to a scale factor of the acceleration different from 1; again, this requires to correct the acceleration-dependent measurements, on the right-hand side of Eq.1. For the reasons above, both inertial and gravitational terms related to the physical scale model, Eq.4 (see Eq.A.4 and A.5) must be subtracted from measurements $\underline{F}_{bal}$ to obtain aerodynamic force vector $\underline{F}_{aero}$ only (Eq.3), to be put in the global equations of motion (Eq.1). The correction force is based on the simulated motions $\underline{x}_s$ instead of the physical ones $\underline{x}$, for a smoother implementation, paying the price of a small (negligible) approximation with respect to relying on the actual motion of the scale model. These aspects and the approach to handle them are reported and thoroughly analysed in [14] and [15].

Hydrodynamic forces Hydrodynamic forces $\underline{F}_{hydro}$ (Eq.5) are computed and combined with aerodynamic forces $\underline{F}_{aero}$ in real time, on right hand-side of Eq.1. The goal is making the computation as fast as possible, finding a balance between the simplification in the modelling and the consistency with the physical phenomena, object of this work.

$$\underline{F}_{hydro} = \underline{F}_{rad} + \underline{F}_{we} + \underline{F}_{visc} + \underline{F}_{moor} \tag{5}$$

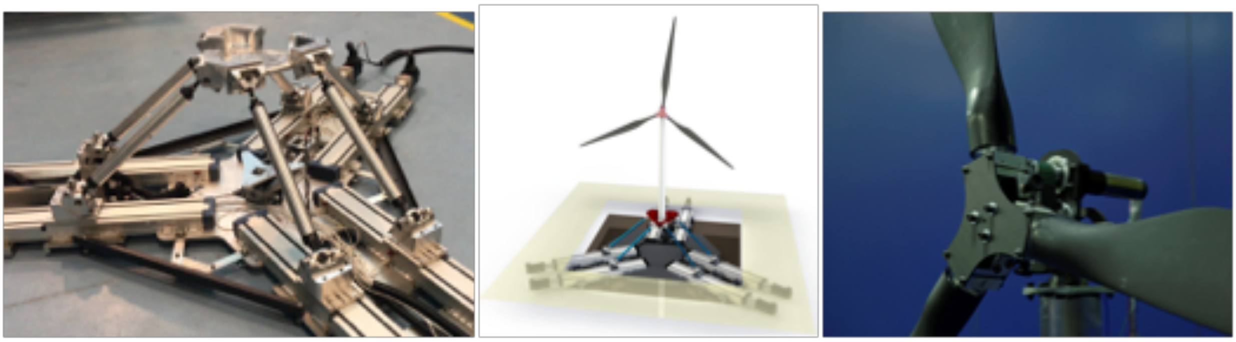

FIGURE 1. Politecnico di Milano 6-DoF Hybrid/HIL setup (center), Hexafloat robot (left) and fully controlled 1/75 aero-elastic scale model of the 10 MW DTU reference wind turbine (right).

Radiation and wave exciting forces Radiation $\underline{F}_{rad}$ and wave exciting $\underline{F}_{we}$ forces are obtained from potential flow problem solved by the 3D panel code WAMIT, [18]. More specifically, $\underline{F}_{rad}$ is implemented under the form of a state-space time domain contribution [19], particularly suited for real-time implementation [20], relying on the frequency-dependent added mass and damping matrices derived from panel code computations. Wave exciting forces $\underline{F}_{we}$ are put in Eq.5 under the form of regular or irregular time histories, see [14].

Viscous Forces As reported in Eq.6, Morison's viscous forces are obtained in the tangential, radial and axial directions, integrating the contribution of single elements along each platform cylinder, depending on the viscous drag coefficients and relative velocities between the wave particle and element's node kinematics, Eq.A.8.

$$\begin{aligned}
F_t(t) &= \int_z f_t(z,t)dz = \int_z \tfrac{1}{2} C_d D \left|v(z)_{rel,t}\right| v(z)_{rel,t} dz \\
F_r(t) &= \int_z f_r(z,t)dz = \int_z \tfrac{1}{2} C_d D \left|v(z)_{rel,r}\right| v(z)_{rel,r} dz \\
F_{ax}(t) &= \int_z f_{ax}(z,t)dz = \int_z \tfrac{1}{2} C_{ax} \pi \tfrac{D^2}{4L} \left|v(z)_{rel,ax}\right| v(z)_{rel,ax} dz
\end{aligned} \tag{6}$$

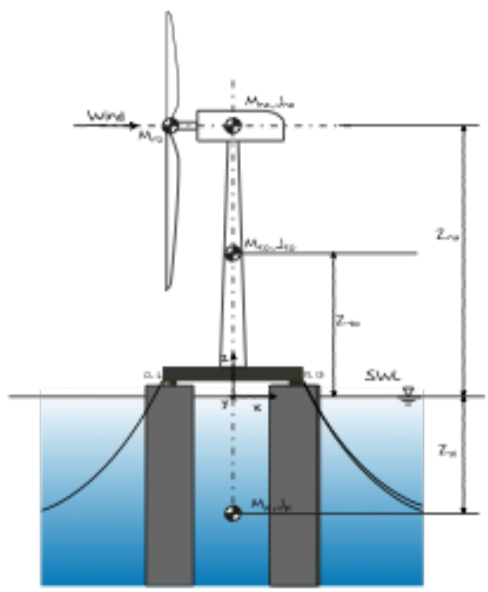

FIGURE 2. Floating system's conventions.

Mooring Forces Mooring lines' forces are taken into account considering the validated formulation in [21], on which the FAST/MoorDyn module is based and whose most relevant elements are herein reported for the sake of clarity. The RT model implements the equations reported in Appendix , although performing specific simplifications, assessed in this paper, mainly due to real-time consistency. The implementation of the complete dynamics of the mooring system was preferred instead of using pre-defined look-up tables adopted for the previous 2 DoF system, [14]. Using look-up tables for the 6 DoF system requires to deploy multidimensional arrays on the HIL real-time controller and the operation turned-out to be unfeasible, both in terms of table dimensions and of look-up operations. Moreover, by using the complete mooring line model it is possible to take into account also velocity-dependent force components resulting in additional linear and quadratic damping for the floating system. The frequency-dependent component of mooring forces cannot be modeled with look-up tables due to quasi-static approach and it has a non-negligible importance in the definition of fatigue loads for the mooring system structural assessment, [22].

After having defined the static equilibrium position, [23], the dynamic response of each element of the catenary, is found by solving the Eq.7, related to a lumped-mass mooring line model, [21]

$$\left[M(\underline{r})\right]\ddot{\underline{r}} = \underline{F}(\underline{r},\dot{\underline{r}}) \tag{7}$$

where a position-dependent overall mass matrix $[M(\underline{r})]$ gives rise to the related inertial forces equilibrated by the corresponding internal forces (Eq.11) of different nature.

$$\left[M(\underline{r})\right] = \left[m\right] + \left[a(\underline{r})\right] \tag{8}$$

The mass of the moorings depend both on the mass of the lines and on the hydrodynamic added mass, as in Eq.8 and Eq.A.9. The added mass is divided into transversal $[a_{p_i}]$ and tangential $[a_{q_i}]$ contributions with respect to the local reference system $(\hat{\underline{q}}_i)$ of each node, approximated through the line passing between two adjacent nodes, Eq.9 and Eq.10, [21].

$$\begin{cases} \left[m_i\right] = \frac{\pi}{4}d^2 l\rho[I]_{3\times3} \\ \left[a_i\right] = [a_{p_i}] + [a_{q_i}] = \\ \quad = \rho_w \frac{\pi}{4}d^2 l\left[C_{an}([I]_{3\times3} - \hat{\underline{q}}_i\hat{\underline{q}}_i^T) + C_{at}(\hat{\underline{q}}_i\hat{\underline{q}}_i^T)\right] \end{cases} \tag{9}$$

$$\hat{\underline{q}}_i = \frac{\underline{r}_{i+1} - \underline{r}_{i-1}}{\|\underline{r}_{i+1} - \underline{r}_{i-1}\|} \tag{10}$$

As reported in Eq.11, the internal nodes of the moorings, contribute in terms of tensile loads $\underline{T}$, damping $\underline{C}$, weight $\underline{W}$, contact with seabed $\underline{B}$ and viscous drag forces $\underline{D}$, see Eq.A.10-A.16.

$$\begin{aligned}\underline{F}(\underline{r},\dot{\underline{r}}) = {} & \underline{T}_{i+1/2}(\underline{r}) - \underline{T}_{i-1/2}(\underline{r}) + \underline{C}_{i+1/2}(\dot{\underline{r}},\underline{r}) - \underline{C}_{i-1/2}(\dot{\underline{r}},\underline{r}) + \\ & + \underline{W}_i + \underline{B}_i(\dot{\underline{r}},\underline{r}) + \underline{D}_{p_i}(\dot{\underline{r}}) + \underline{D}_{q_i}(\dot{\underline{r}})\end{aligned} \tag{11}$$

The integration of Eq.7 allows to define, at each time step, the dynamics of the nodes $(\underline{r},\dot{\underline{r}})$ and to compute the overall mooring line forces $\underline{F}_{moor}$ at the fairleads, Eq.12.

$$\underline{F}_{moor}(\underline{r},\dot{\underline{r}}) = -\underline{T}_N - \underline{C}_N + \underline{W}_N + \underline{D}_{p_N} + \underline{D}_{q_N} \tag{12}$$

OPTIMIZATION FOR REAL-TIME IMPLEMENTATION

The optimization of the real time model reported in Eq.1 results in a consistent reduction of the number of computations and operations executed during the Hybrid/HIL tests with regard to the hydrodynamic forces $\underline{F}_{hydro}$, generally not required adopting usual numerical engineering tools, [24]. This optimization can be roughly summarized in the reduction of: *(I)* the number of harmonics considered in the spectrum of the irregular sea state simulations ($\underline{F}_{we}$); *(II)* the number of elements dividing the substructure $\underline{F}_{visc}$; *(III)* the number of *nodes* composing the mooring lines and *(IV)* the choice of specific contributions in terms of forces to be considered from the internal nodes of the catenary and *(V)* general implementation issues.

(I) The number of harmonic components in the spectrum and its frequency resolution is of critical decision and it can't be kept the same as in off-line simulations (i.e. FAST). A compromise between physical consistency and computational effort must be reached. It was found that decreasing the frequency resolution by 10 times from FAST simulations to HIL implementation was guaranteeing this balance, so that a $\Delta\omega = 0.002$ rad/s was turned to $\Delta\omega = 0.02$ rad/s keeping satisfactory results. With regard to linear spectrum simulation a range of 0.3-3.3 rad/s was considered sufficiently representative, being the significant contribution of the adopted JONSWAP spectrum falling within this range.

(II) The viscous forces depend on the relative velocity between the platform and water (Eq.A.8). Nevertheless the wave particle speed decreases exponentially [25], and it is acceptable

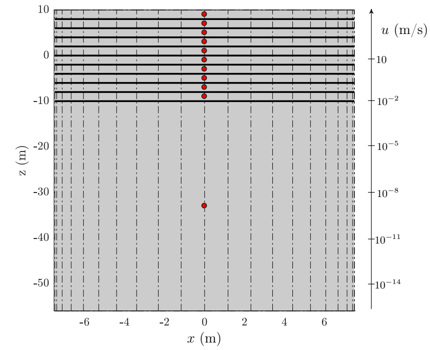

FIGURE 3. Optimal discretization of the Triple Spar platform cylinder (Fig.2) for Morison's viscous force $\underline{F}_{hydro}$ computation.

	10^7 (N) HIL	10^7 (Nm) FAST
$\mathbf{F_x}$	0.0548	0.0548
$\mathbf{M_y}$	1.8727	1.8657

TABLE 2. Comparison (amplitudes) of the most relevant Morison's forces for a regular sea state between the optimized model (HIL, Fig.3) and the reference one (FAST) with finer discretization. Wave height 2.2 m and period 8 s.

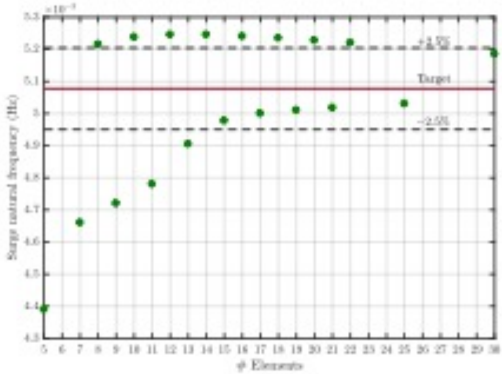

FIGURE 4. Sensitivity analysis of the effect of the mooring's discretization on the natural frequency of the system (surge).

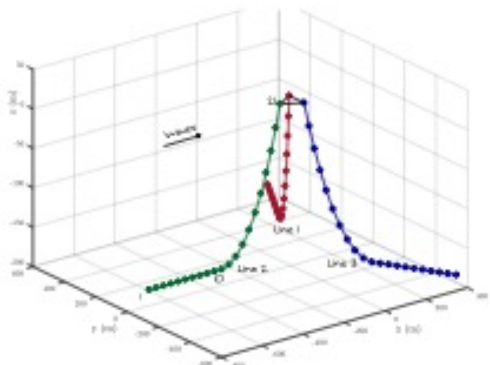

FIGURE 5. Mooring line system's optimal discretization.

to reduce the number of nodes in the lower part of the platform where the velocity gradient is lower. The optimal discretization of the platorm's cylinder is reported in Fig.3, showing the order of magnitude of the along-wave particle horizontal velocity u. The choice of considering a single element in a quite large area of substructure is consistent both with the effective wave velocity and with the low speed gradient, allowing to diminish a relevant number of operations. This is confirmed by the overall viscous forces reported in Tab.2 for a sample regular wave case, along with the results on the decay tests reported and discussed in the following (Fig.11).

(III) The number of nodes in the mooring lines were optimized considering as target the system's natural frequencies provided by decay simulation obtained with reference FAST/MoorDyn model with 100 nodes. As visible from Fig.4, an optimal number of 21 elements, including the anchor point and the fairlead, allows to reach a good compromise, resulting in

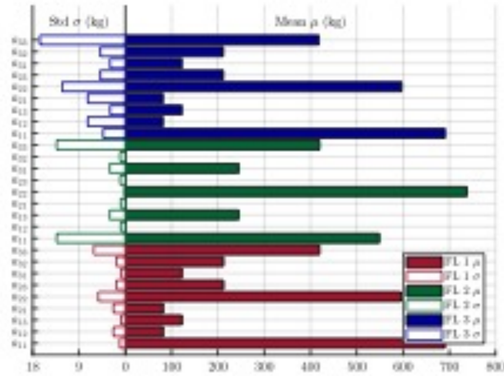

FIGURE 6. Added mass $[a_i]$ contribution (Eq.9) for the node # 20 for the combined decay tests $\underline{x} = \{x, y, z, \varphi, \vartheta, \psi\}^T = \{20\,m, 20\,m, 10\,m, 15^\circ, 15^\circ, 15^\circ\}^T$.

natural frequencies within 2% of discrepancy with respect to the target. The corresponding optimal layout is reported in Fig.5.

(IV) Considering a combined decay with the given initial conditions $\underline{x} = \{x, y, z, \varphi, \vartheta, \psi\}^T = \{20\,m, 20\,m, 10\,m, 15^\circ, 15^\circ, 15^\circ\}^T$ each contribution on internal nodes of the mooring line (Eq.11) was investigated individually to discern the most relevant ones.

In Fig.6 the mean values μ and standard deviation σ are reported for the $[a_i]$ matrix elements of the node experiencing the largest amplitude of motion (#20). It can be seen how small is the variation of these elements, allowing to consider the added mass of the mooring system in $[M]$ (Eq.A.2 and Eq.A.9) constant over the HIL tests, thus reducing the computational effort. In-fact, Eq.A.9 is not required to be inverted at each time step but only during in the preliminary phase defining the mooring steady condition, [23].

Fig.7-10, show statistical values (standard deviation σ and mean μ when different from 0) for the different mooring contributions in Eq.11 every are reported for the internal nodes (#2-20).

Regarding viscous forces $\underline{D}$, it must be specified that this analysis was carried out in still water (decay), consistent with the reference FAST/MoorDyn module, in which no relative velocity of the elements is considered for these computations, but only the velocity due to the elements themselves. As it is reasonable, Fig.7 shows that only the nodes off the seabed (i.e. #$\geq$10, Fig.5) are worth being considered in the computation of this force contribution, saving a great amount of useless operations by neglecting nodes on the seabed. On the contrary, from Fig.8 it is visible that the contribution of the seabed contact $\underline{B}$ (Eq.A.16) can be divided into constant elements, related to the very first nodes close to the anchors, then intermediate nodes with varying contribu-

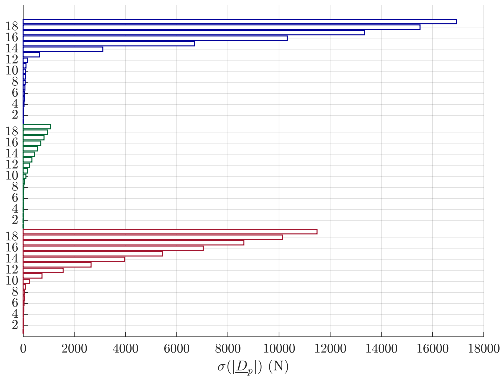

FIGURE 7. Viscous transverse damping D_p contribution (Eq.11) for the internal nodes (#2-20) in the combined decay tests $\underline{x} = \{x, y, z, \varphi, \vartheta, \psi\}^T = \{20\,m, 20\,m, 10\,m, 15°, 15°, 15°\}^T$.

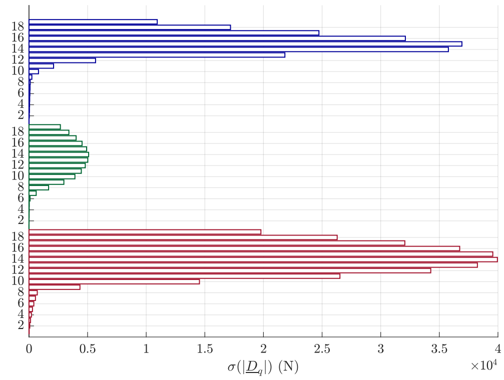

FIGURE 9. Viscous tangential damping D_q contribution (Eq.11) for the internal nodes (#2-20) in the combined decay tests $\underline{x} = \{x, y, z, \varphi, \vartheta, \psi\}^T = \{20\,m, 20\,m, 10\,m, 15°, 15°, 15°\}^T$.

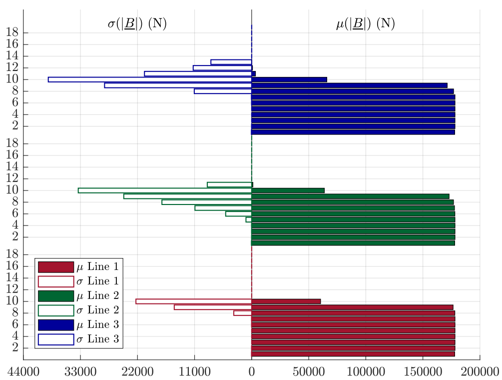

FIGURE 8. Seabed contact contribution B (Eq.11) for the internal nodes (#2-20) in the combined decay tests $\underline{x} = \{x, y, z, \varphi, \vartheta, \psi\}^T = \{20\,m, 20\,m, 10\,m, 15°, 15°, 15°\}^T$.

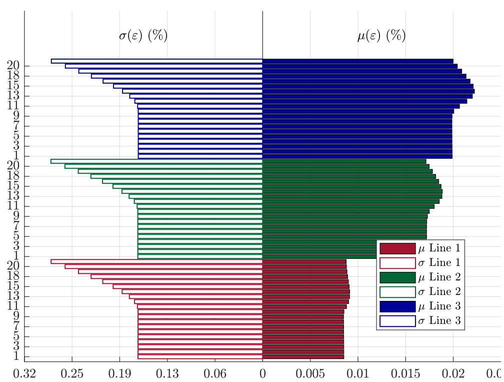

FIGURE 10. ε contribution (Eq.11) for the internal nodes (#2-20) in the combined decay tests $\underline{x} = \{x, y, z, \varphi, \vartheta, \psi\}^T = \{20\,m, 20\,m, 10\,m, 15°, 15°, 15°\}^T$.

tion (i.e. nodes # 6-14) that can happen to be in contact with the seabed, then nodes up to the farileads (# 21) which can be completely avoided from the calculation.

With regard to the contribution to the stiffness due to the axial tensile load $\underline{T}$ and damping $\underline{C}$, the strain for each node was investigated for the decay tests and is reported in Fig.10, where it can be seen how axial stretch changes are small (lower than 1%) during the platform's motion, suggesting to set these contributions as constant. This cannot be done since the model encounters convergence issues otherwise.

The above considerations are summarized in Tab.3, reporting the final modelling scheme for the mooring lines.

(V) Many technical/implementation issues arise in the presented real-time modelling; the most relevant ones, which have affected greatly the real time modelling approach, are herein reported. Regarding the integration time step, the mooring lines represent the most binding part of the modelling, requiring a well finer discretization compared to the rest of the model; this is reflected also in the reference FAST/MoorDyn module. An acceptable compromise was found for this floating concept to be of 0.02 s full scale, resulting in a time step around 8e-4 s at model scale, associated with an ODE45 integration scheme.

For the same reasons that led to a comprehensive real-time implementation of the mooring line dynamics, the first and second order wave exciting forces $\underline{F}_{we}$ are computed at each time step spanning over the wave frequency range, relying on the

	1	2	3	4	5	6	7	8	9	10	11	12	13	14	15	16	17	18	19	20	21
M	$\underline{\triangle}$	—	—	—	—	—	—	—	—	—	—	—	—	—	—	—	—	—	—	—	$\triangle$
$\underline{T}$	$\underline{\triangle}$	$\color{red}{-}$	$\color{red}{-}$	$\color{red}{-}$	$\color{red}{-}$	$\color{red}{-}$	$\color{red}{-}$	$\color{red}{-}$	$\color{red}{-}$	$\color{red}{-}$	$\color{red}{-}$	$\color{red}{-}$	$\color{red}{-}$	$\color{red}{-}$	$\color{red}{-}$	$\color{red}{-}$	$\color{red}{-}$	$\color{red}{-}$	$\color{red}{-}$	$\color{red}{-}$	$\triangle$
$\underline{C}$	$\underline{\triangle}$	$\color{red}{-}$	$\color{red}{-}$	$\color{red}{-}$	$\color{red}{-}$	$\color{red}{-}$	$\color{red}{-}$	$\color{red}{-}$	$\color{red}{-}$	$\color{red}{-}$	$\color{red}{-}$	$\color{red}{-}$	$\color{red}{-}$	$\color{red}{-}$	$\color{red}{-}$	$\color{red}{-}$	$\color{red}{-}$	$\color{red}{-}$	$\color{red}{-}$	$\color{red}{-}$	$\triangle$
$\underline{D}_p$	$\underline{\triangle}$	✗	✗	✗	✗	✗	✗	✗	✗	✓	✓	✓	✓	✓	✓	✓	✓	✓	✓	✓	$\triangle$
$\underline{D}_q$	$\underline{\triangle}$	✗	✗	✗	✗	✗	✗	✗	✗	✓	✓	✓	✓	✓	✓	✓	✓	✓	✓	✓	$\triangle$
$\underline{B}$	$\underline{\triangle}$	—	—	—	—	✓	✓	✓	✓	✓	✓	✓	✓	✓	✗	✗	✗	✗	✗	✗	$\triangle$

TABLE 3. Summary of the inclusion of the various mooring line's force contributions of the internal nodes, from anchor ($\underline{\triangle}$) to fairlead ($\triangle$): constant nodes (—), potentially constant ($\color{red}{-}$), varying (✓) and neglected (✗).

	f (Hz) HIL	f (Hz) FAST	p HIL	p FAST	q HIL	q FAST
Surge	0.0052	0.0050	0.24	0.28	0.039	0.033
Sway	0.0049	0.0049	0.26	0.30	0.034	0.028
Heave	0.0628	0.0628	0.31	0.31	0.015	0.015
Roll	0.0360	0.0361	0.38	0.32	-0.059	-0.018
Pitch	0.0380	0.0380	0.35	0.29	-0.037	0.001
Yaw	0.0130	0.0130	0.10	0.10	0.014	0.017

TABLE 4. Summary of the comparison between the real-time HIL model and the reference FAST model, including the natural frequencies f, the linear and quadratic damping parameters p and q.

complex frequency dependent vectors given by WAMIT. This was preferable instead of entering pre-defined heavy multidimensional lookup tables returning forces for each time step.

The computation of the wave kinematics u,v,w could be theoretically computed off-line in advance, saving computation and time at each step of the simulations, since they do not depend on the floating system. Nevertheless, the Wheeler function adopted to compute the velocities, [25], takes into account also the wave stretching above the SWL, which in turns depends on the vertical platform position, making the off-line determination of this contribution not possible.

RESULTS AND CONCLUSIONS

In Fig.11 and Fig.12 the free decay and irregular sea results (without wind) are reported to compare the HIL model to the reference FAST one, for a subset of selected DoF, that are those envisaging the most significant amplitudes. The HIL model shows an almost overlapped behaviour. The same conclusions can be drawn looking at Tab.4, which reports the corresponding natural frequencies, linear and quadratic damping p and q, respectively defined as intercepts and slope of the graph $\frac{\Phi_n-\Phi_{n+1}}{1/2(\Phi_n+\Phi_{n+1})}$ Vs $\frac{1}{2}(\Phi_n+\Phi_{n+1})$, being Φ_n and $+\Phi_{n+1}$ the peaks of two consequent cycles of the DoF, as defined in [26]. Tab.4 confirms the correctness of the procedure reported, where very close values between HIL and FAST can be seen. This confirms that the sensitivity analysis conducted in the definition of the real-time model, with the burden of selecting the contributions that are actually relevant from an engineering point of view, can be considered satisfactory. Furthermore, following this preliminary analysis, ongoing assessments are being focused on different floating platforms and different sea-conditions contributing to make this methodology more robust; more comprehensive numerical and experimental analysis are expected to be published soon.

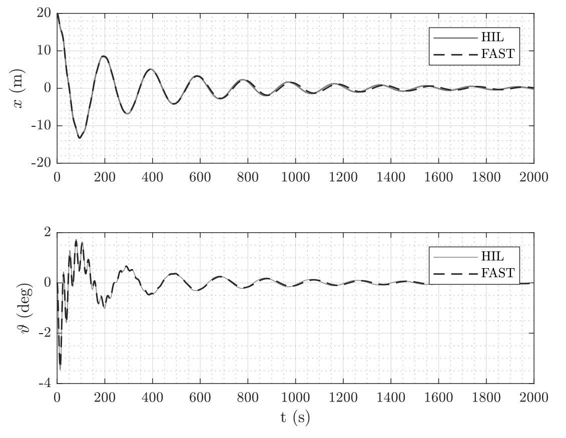

FIGURE 11. Surge x and pitch ϑ decay comparison.

ACKNOWLEDGMENT

This project has partially received funding from the European Unions Horizon 2020 research and innovation programme under grant agreement No 640741. The authors want also to ac-

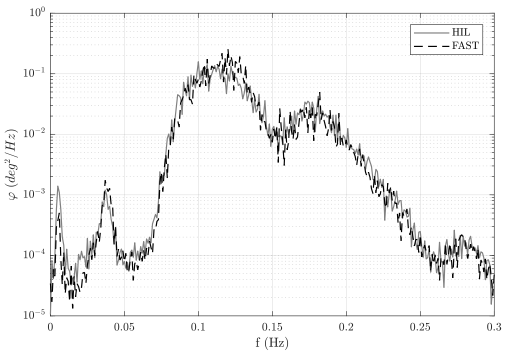

FIGURE 12. Pitch ϑ PSD comparison for irregular sea, $H_s = 2.2m$ and $T_p = 8s$.

knowledge the master student Lorenzo Delbene, for his help in the implementation of the model during his thesis work.

REFERENCES

[1] Jain, A., Robertson, A., Jonkman, J., Goupee, A., Kimball, R., and Swift, A., 2012. "Fast code verification of scaling laws for deepcwind floating wind system tests". pp. 355–365.

[2] Robertson, A., Jonkman, J., Goupee, A., Coulling, A., Prowell, I., Browning, J., Masciola, M., and Molta, P., 2013. "Summary of conclusions and recommendations drawn from the deepcwind scaled floating offshore wind system test campaign". Vol. 8.

[3] H2020 LIFES50+ project. http://lifes50plus.eu/.

[4] Sauder, T., Chabaud, V., Thys, M., Bachynski, E., and Sæther, L., 2016. "Real-time hybrid model testing of a braceless semi-submersible wind turbine. part I: The hybrid approach". In Proceedings of the International Conference on Offshore Mechanics and Arctic Engineering - OMAE, Vol. 6.

[5] Azcona, J., Bouchotrouch, F., Gonzlez, M., Garcianda, J., Munduate, X., Kelberlau, F., and Nygaard, T., 2014. "Aerodynamic thrust modelling in wave tank tests of offshore floating wind turbines using a ducted fan". *Journal of Physics: Conference Series,* ***524***(1).

[6] Bayati, I., Belloli, M., Ferrari, D., Fossati, F., and Giberti, H., 2014. "Design of a 6-DoF robotic platform for wind tunnel tests of floating wind turbines". In Energy Procedia, Vol. 53.

[7] Bachynski, E., Thys, M., Sauder, T., Chabaud, V., and Sæther, L., 2016. "Real-time hybrid model testing of a braceless semi-submersible wind turbine. part II: Experimental results". In Proceedings of the International Conference on Offshore Mechanics and Arctic Engineering - OMAE, Vol. 6.

[8] Bayati, I., Belloli, M., Bernini, L., Giberti, H., and Zasso, A., 2017. "Scale model technology for floating offshore wind turbines". *IET Renewable Power Generation,* ***doi:10.1049/iet-rpg.2016.0956***.

[9] Politecnico di milano wind tunnel (GVPM). http://www.windtunnel.polimi.it/.

[10] Bayati, I., Belloli, M., Bernini, L., and Zasso, A., 2017. "Aerodynamic design methodology for wind tunnel tests of wind turbine rotors". *Journal of Wind Engineering and Industrial Aerodynamics,* ***167***, pp. 217–227.

[11] Bayati, I., Belloli, M., Bernini, L., Fiore, E., Giberti, H., and Zasso, A., 2016. "On the functional design of the DTU10 MW wind turbine scale model of LIFES50+ project". *Journal of Physics: Conference Series,* ***753***(5).

[12] Fontanella, A., Bayati, I., and Belloli, M., 2018. "Control of floating offshore wind turbines: Reduced-order modelling and real-time implementation for wind tunnel tests". In Proceedings of the International Conference on Offshore Mechanics and Arctic Engineering - OMAE, no. OMAE2018-77840.

[13] Giberti, H., Fiore, E., and Saccomani, A., 2018. "On the mechatronic design of a low-cost 6-dofs parallel kinematic manipulator". *Mechanisms and Machine Science,* ***49***, pp. 46–54.

[14] Bayati, I., Belloli, M., and Facchinetti, A., 2017. "Wind tunnel 2-DoF hybrid/hil tests on the OC5 floating offshore wind turbine". *36th International Conference on Ocean, Offshore and Arctic Engineering, Trondheim (Norway), 2017,* ***OMAE2017-61763***.

[15] Ambrosini, S., Bayati, I., Belloli, M., and Facchinetti, A., 2017. "Methodological and technical aspects of a 2DoF/HIL setup for wind tunnel tunnel tests of floating systems". *Journal of Dynamic Systems, Measurement, and Control*.

[16] Bredmose, H., Lemmer, F., Borg, M., Pegalajar-Jurado, A., Mikkelsen, R., Larsen, T. S., Fjelstrup, T., Yu, W., Lomholt, A., Boehm, L., and Armendariz, J. A., 2017. "The triple spar campaign: Model tests of a 10mw floating wind turbine with waves, wind and pitch control". *Energy Procedia,* ***137***, pp. 58 – 76.

[17] Bak, C., 2013. "The DTU 10-MW reference wind turbine". *Technical University of Denmark, DTU Wind Energy*.

[18] Lee, C., 1995. "WAMIT theory manual". *Department of Ocean engineering, Massachusetts Institute of Technology*.

[19] Duarte, T., Alves, M., Jonkman, J., and Sarmento, A., 2013. "State-space realization of the wave-radiation force within fast". Vol. 8.

[20] Duarte, T. *SS Fitting, Theory and User Manual*.

[21] Hall, M., and Goupee, A., 2015. "Validation of a lumped-

mass mooring line model with deepcwind semisubmersible model test data". *Ocean Engineering,* ***104***, pp. 590–603.
[22] Wendt, F., Robertson, A., Jonkman, J., and Andersen, M. T., 2016. "Verification and validation of the new dynamic mooring modules available in fast v8". *Proceedings of the Twenty-sixth International Ocean and Polar Engineering Conference (ISOPE).*
[23] Masciola, M., Jonkman, J., and Robertson, A., 2013. "Implementation of a multisegmented, quasi-static cable model". pp. 315–322.
[24] Jonkman, M. L. B. J., 2005. "Fast user's guide".
[25] J.N.Newman, 1977. *Marine Hydrodynamics*.
[26] Helder, J., and Pietersma, M. Umaine deepcwind/oc4 semi floating wind turbine repeat tests. Tech. rep., MARIN.

Appendix: Analytics

$$[M_s] = \begin{bmatrix} M_{tot} & 0 & 0 & 0 & M_{ed} & 0 \\ 0 & M_{tot} & 0 & -M_{ed} & 0 & 0 \\ 0 & 0 & M_{tot} & 0 & 0 & 0 \\ 0 & -M_{ed} & 0 & M_{44} & 0 & 0 \\ M_{ed} & 0 & 0 & 0 & M_{55} & 0 \\ 0 & 0 & 0 & 0 & 0 & M_{66} \end{bmatrix} \tag{A.1}$$

$$\begin{aligned} M_{tot} &= M_{pl} + M_{to} + M_{na} + M_{ro} \\ M_{ed} &= M_{pl}Z_{pl} + M_{to}Z_{to} + (M_{na} + M_{ro})Z_{na} \\ M_{44} &= Jx_{pl} + Jx_{to} + M_{pl}Z_{pl}^2 + M_{to}Z_{to}^2 + (M_{na} + M_{ro})Z_{na}^2 \\ M_{55} &= Jy_{pl} + Jy_{to} + M_{pl}Z_{pl}^2 + M_{to}Z_{to}^2 + (M_{na} + M_{ro})Z_{na}^2 \\ M_{66} &= Jz_{pl} + Jz_{to} + Jz_{na} \end{aligned} \tag{A.2}$$

$$\begin{aligned} |v_{G,xz}|^2 &= \dot{x}^2 + l_G^2\dot{\vartheta}^2 + 2l_G\dot{x}\dot{\vartheta} \\ |v_{G,yz}|^2 &= \dot{y}^2 + l_G^2\dot{\varphi}^2 - 2l_G\dot{y}\dot{\varphi} \end{aligned} \tag{A.3}$$

$$[M_t] = \begin{bmatrix} m_t & 0 & 0 & 0 & m_t b_z & 0 \\ 0 & m_t & 0 & -m_z b_z & 0 & -m_t b_x \\ 0 & 0 & m_t & 0 & 0 & 0 \\ 0 & -m_t b_z & 0 & J_{xx} & 0 & J_{xz} \\ m_t b_z & 0 & 0 & 0 & J_{yy} & 0 \\ 0 & -m_t b_x & 0 & J_{xz} & 0 & J_{zz} \end{bmatrix} \tag{A.4}$$

$$[K_t] = \begin{bmatrix} 0\,0\,0 & 0 & -m_t g & 0 \\ 0\,0\,0 & m_t g & 0 & 0 \\ 0\,0\,0 & 0 & 0 & 0 \\ 0\,0\,0 & -m_t b_z g & 0 & 0 \\ 0\,0\,0 & 0 & -m_t b_z g & 0 \\ 0\,0\,0 & 0 & 0 & 0 \end{bmatrix} \tag{A.5}$$

$$k_{grav} = g(M_{pl}Z_{pl} + M_{to}Z_{to} + (M_{na} + M_{ro})Z_{na}) \tag{A.6}$$

$$[K_{grav}] = \begin{bmatrix} 0\,0\,0 & 0 & 0 & 0 \\ 0\,0\,0 & 0 & 0 & 0 \\ 0\,0\,0 & 0 & 0 & 0 \\ 0\,0\,0 & k_{grav} & 0 & 0 \\ 0\,0\,0 & 0 & k_{grav} & 0 \\ 0\,0\,0 & 0 & 0 & 0 \end{bmatrix} \tag{A.7}$$

$$\begin{cases} v_{x,rel}(z,t) = u(z,t) - v_{x,pl}(z,t) \\ v_{y,rel}(z,t) = v(z,t) - v_{y,pl}(z,t) \\ v_{z,rel}(z,t) = w(z,t) - v_{z,pl}(z,t) \end{cases} \tag{A.8}$$

$$[M] = \begin{bmatrix} [m_1]+[a_1] & & & & \\ & \ddots & & & \\ & & [m_i]+[a_i] & & \\ & & & \ddots & \\ & & & & [m_N]+[a_N] \end{bmatrix} \tag{A.9}$$

$$W_{i+1/2} = \frac{\pi}{4}d^2 l(\rho_w - \rho)g; \underline{W}_i = \frac{1}{2}(W_{i+1/2} + W_{i-1/2})\underline{\hat{e}}_z \tag{A.10}$$

$$\underline{T}_{i+1/2} = E\frac{\pi}{4}d^2\left(\frac{1}{l} - \frac{1}{\|\underline{r}_{i+1} - \underline{r}_i\|}\right)(\underline{r}_{i+1} - \underline{r}_i) \tag{A.11}$$

$$\underline{C}_{i+1/2} = C_{int}\frac{\pi}{4}d^2\dot{\varepsilon}_{i+1/2}\left(\frac{\underline{r}_{i+1} - \underline{r}_i}{\|\underline{r}_{i+1} - \underline{r}_i\|}\right) \tag{A.12}$$

$$\dot{\varepsilon}_{i+1/2} = \frac{\partial}{\partial t}\varepsilon_{i+1/2} = \frac{\partial}{\partial t}\left(\frac{\|\underline{r}_{i+1} - \underline{r}_i\|}{l}\right) \tag{A.13}$$

$$\underline{D}_{p_i} = \frac{1}{2}\rho_w C_{dn} dl \left\| (\underline{\dot{r}}_i \cdot \underline{\hat{q}}_i)\underline{\hat{q}}_i - \underline{\dot{r}}_i \right\| ((\underline{\dot{r}}_i \cdot \underline{\hat{q}}_i)\underline{\hat{q}}_i - \underline{\dot{r}}_i) \tag{A.14}$$

$$\underline{D}_{q_i} = \frac{1}{2}\rho_w C_{dt} \pi dl \left\| (-\underline{\dot{r}}_i \cdot \underline{\hat{q}}_i)\underline{\hat{q}}_i \right\| (-\underline{\dot{r}}_i \cdot \underline{\hat{q}}_i)\underline{\hat{q}}_i \tag{A.15}$$

$$\underline{B}_i = dl[(z_{bot} - z_i)k_{bot} - \dot{z}_i c_{bot}]\underline{\hat{e}}_z \tag{A.16}$$